NUMERICAL AND EXPERIMENTAL EVALUATION OF ADHESIVELY BONDED, LARGE SCALE, FULL COMPOSITE JOINTS IN MARITIME APPLICATIONS

Teodor Gheorghe; Bilim Atli-Veltin; Michiel Hagenbeek; Jan Peeters; Marcel Elenbaas

[1] Oostdijk 25, 3077CP, Rotterdam, The Netherlands, TU Delft/TNO/InfraCore Company (ICC), gheorghe@infracore-company.com
[2]Kluyverweg 1, 2629 HS Delft, The Netherlands, TU Delft/TNO, b.atli-veltin-1@tudelft.nl
[3]Leeghwaterstraat 44, 2628 CA Delft, The Netherlands, TNO, michiel.hagenbeek@tno.nl
[4]Oostdijk 25, 3077CP, Rotterdam, The Netherlands, ICC, peeters@infracore-company.com
[5] De Willem Ruysstraat 99, 4381 NK Vlissingen, The Netherlands, Damen Schelde Naval Shipbuilding (DSNS), m.elenbaas@damennaval.com

Keywords: Composite panels, Finite Element Analysis, Damage propagation, Adhesive joints, Interlaminar damage

ABSTRACT

Composite materials have a wide range of uses in engineering applications. Their ever-growing implementation stems from their advantages including high strength, durability, and lightweight. However, especially in highly loaded maritime composite structures challenges still exist. [1].

One of the aims of the RAMSSES European project is to tackle the challenges of designing and building an 85 m-long full composite vessel that complies with Safety of Life at Sea (SOLAS) and Class regulations [2]. With this goal in mind, a section of a custom ship, including three novel joint designs, is conceptualized. These connections are full composite joints, and they connect the heavily loaded deck to the bulkheads and to the ship hull. Novelty comes from the fact that no metal is used in these connections since panels are adhesively bonded, bringing the weight even lower compared to current examples of such joints which include metal fasteners [3]. Such joints have other disadvantages such as complex assembly and corrosion issues which require additional measures such as coatings or other forms of conservation to ensure functionality. The performance evaluation of these joints is the topic of this paper.

Three different joint types were proposed that, according to the analytical and finite element calculations, surpassed the performance required by the initial ship design. Subsequently, they were built to scale and tested in a bending configuration that introduces a loading condition, similar to that of the real structure.

Non-crimp glass fiber fabrics in combination with toughened vinylester resin were used in Vacuum Assisted Resin Transfer Molding (VARTM) process to produce the joint components and methyl-methacrylate (MMA) adhesive was used for the bonding process. For each joint type three specimens were produced and tested. A failure prediction model was built in Abaqus for each joint type and the performance was validated against the experimental results.

1 INTRODUCTION

Composite or Fiber Reinforced Polymer (i.e. FRP) materials have a wide range of use in various domains. Their ever-growing implementation stems from their advantages including high strength, durability, and lightweight. However, especially in the maritime sector, composite structures still face challenges [1]. In this regard, RAMSSES European project focuses on designing and building a full composite vessel that complies with Safety of Life at Sea (SOLAS) and Class regulations [2], [3]. As a part of this project, a section of a custom ship with three novel joint designs is conceptualized. These connections are full composite connecting the heavily loaded deck to the bulkheads and to the ship hull, as shown schematically in Figure 1. In this figure, the top deck breadth is 14 m, which gives a sense of scale for how big the considered ship is.

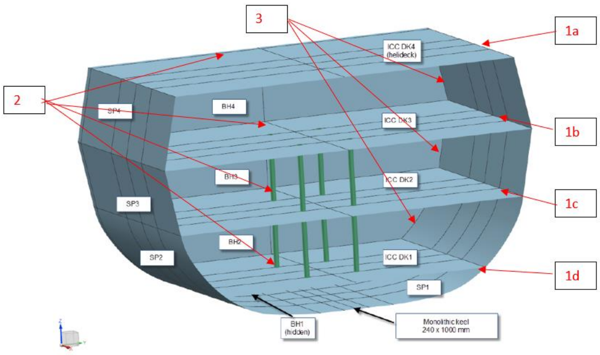

Figure 1 – Simplified section view of the designed ship; From bottom to top: Deck 1 to 4

Novelty of the current research mainly comes from the large size of the joints considered and the fact that no metal is used in these connections. Current examples of such joints typically include metal components and fasteners [4]. In addition to their weight penalty, metal joints have disadvantages such as design and assembly complexities, corrosion issues which require additional measures such as coatings or other forms of protection to ensure functionality. Full adhesive composites joints applied in the maritime field have been investigated by a limited number of researchers. In 2018, Zeng et al [5] looked at large scale, bonded joints in which sandwich panels representing the deck and hull were bonded together and strengthened by L-shaped stiffeners, also made of composites. The typical approach to evaluate the performance of new designs includes carrying out numerous small or large scale experiments and developing a validated numerical model with the aim of subjecting the numerical model to many scenarios to identify potential weaknesses or predict failure loads and mechanisms. A similar approach is followed in the current work, covering experimental campaigns and numerical modelling. The current paper provides details of the test articles, test conditions, experimental and numerical results.

2 EXPERIMENTAL INVESTIGATION

Considered joint configurations were designed with the aim to combine the simplicity with functionality while relying on almost perfect hinge-like behaviour for the load transfer. This implies that minimal bending moments are transferred to the adjacent panels (i.e. from deck to hull). The locations of the considered joints on the ship section are highlighted in Figure 1; joint 1a to 1d refers to deck-to-hull connections; joint 2 refers to deck-to-bulkhead connections; and joint 3 refers to hull-to-bulkhead connections. RAMSSES project partner Damen Schelde Naval Shipbuilding [6] provided a simplified global design of the ship as well as the input for the detailed joint design, namely the deflections of the panels, the shear and bending loads along the interfaces. Taking into this information, three different joint types are designed and produced by RAMSSES project partner InfraCore Company [7]. Subsequently, the built-to-scale specimens are tested in bending at RAMSSES project partner TNO introducing a loading condition that is similar to that of the real structure. The production and testing of the three different joint types are detailed in the following sub-chapters.

2.1 Specimen design and manufacturing

Figure 2 shows the geometry of the specimens, hereby named Type A, B and C, that are tested in the current research. Joints Type A and B are similar in terms of load transfer mechanism. The load is primarily transferred in shear by the adhesive bond. Joint Type C combines adhesive bonding with shape locking to provide an increased capacity, and improved durability, as required by the type of panels that it connects (i.e. deck to hull) and the magnitude of the load that needs to be transferred.

The specimens are designed to be a 1:1 scale representation of the component in terms of laminate thicknesses, web spacing and joint geometry. On average, the width of the specimen is ~1200 mm and the height is 1000 mm. The specimens are designed to be symmetric to facilitate testing. The panels are sandwich structures, manufactured using non-crimp glass fibre fabrics in combination with Evonik Albidur Hull VE toughened vinylester resin in Vacuum Assisted Resin Transfer Moulding (VARTM) infusion process. Bonding of the components is done using Scigrip SG300 methyl-methacrylate (MMA). Production is done in typical factory conditions to obtain build quality similar to that of a real structure.

The layups for the laminates are carefully designed by InfraCore to account for the respective load directions and magnitudes. The outcome is that the decks and bulkheads have 70% fibres in the 0-degree direction (i.e. in the joint direction, see Figure 2) and 30% equally distributed in +/-45-degree directions, while the hull has a quasi-isotropic layup (i.e. equal number of fibres in 0/90/45/-45-degree directions). The products are cured at room temperature, as per the manufacturer's specifications. Following the panel production, the next step is bonding to create the joints. Surface preparation of the bonding surfaces is done according to the recommendations of the adhesive manufacturer. These included removing the peel ply, cleaning of dust with clean cloth and degreasing the surface with acetone. The bonding process consists of two steps. The first step involves using a 5-minute cure variant of the adhesive to apply a seal along three sides of each joint, while the second step consists of filling of the cavity with the 40-minute variant. The ends of the bond line are provided with fillets to reduce the stress concentrations. The maximum bond thickness is ~ 8mm with a ± 1mm tolerance due to uneven surfaces and misalignments.

2.2 Testing procedure and setup

The test is performed, in a 5-point-bending configuration in a custom test bench using MTS load cell and software. The setup is designed such that the load is applied at the centre of the specimen, and then it is transferred through the adhesive joints, to the two support rollers on either side (see Figure 3). The positions of the supports are determined based on the rotation that occurs at maximum displacement in the full model of the ship. The test span (the distance between the centre of the right to the centre of the left support) lengths are for Joint Type A: 750 mm, Joint Type B: 325 mm, and Joint Type C: 450 mm.

The two additional upper supports are there to provide a limit for the amount of rotation the joint is allowed to experience. This is necessary to ensure a correct load introduction into the joint, otherwise too large rotations cause significantly more bending moment to be transferred and not enough shear load. This can result in undesired failure modes that do not represent the real-case use of the joint in the structure.

The loads to be applied to the joints are determined following the Bureau Veritas [3] regulations which prescribe that the joints should be successfully tested at a load value that is six times the design load if failure occurs in the composite part, or ten times the design load if failure occurs in the adhesive. If the joints do not fail at that load in static testing, no additional fatigue verification is necessary.

The force is applied in displacement control The application rate is 2mm/min for Type A and B and 5mm/min for joint Type C. The load is applied in displacement control. The magnitude of the load cell (see Figure 4) is chosen to be 100kN. The test is performed in the static regime, up to failure, without reloading. Additional calculations are made to ensure that no undesired failure modes due to load introduction can occur (i.e. buckling of laminates of central component or compressive failure). Local damage on the side components due to localised load introduction is not considered to be relevant for the performance of the joint.

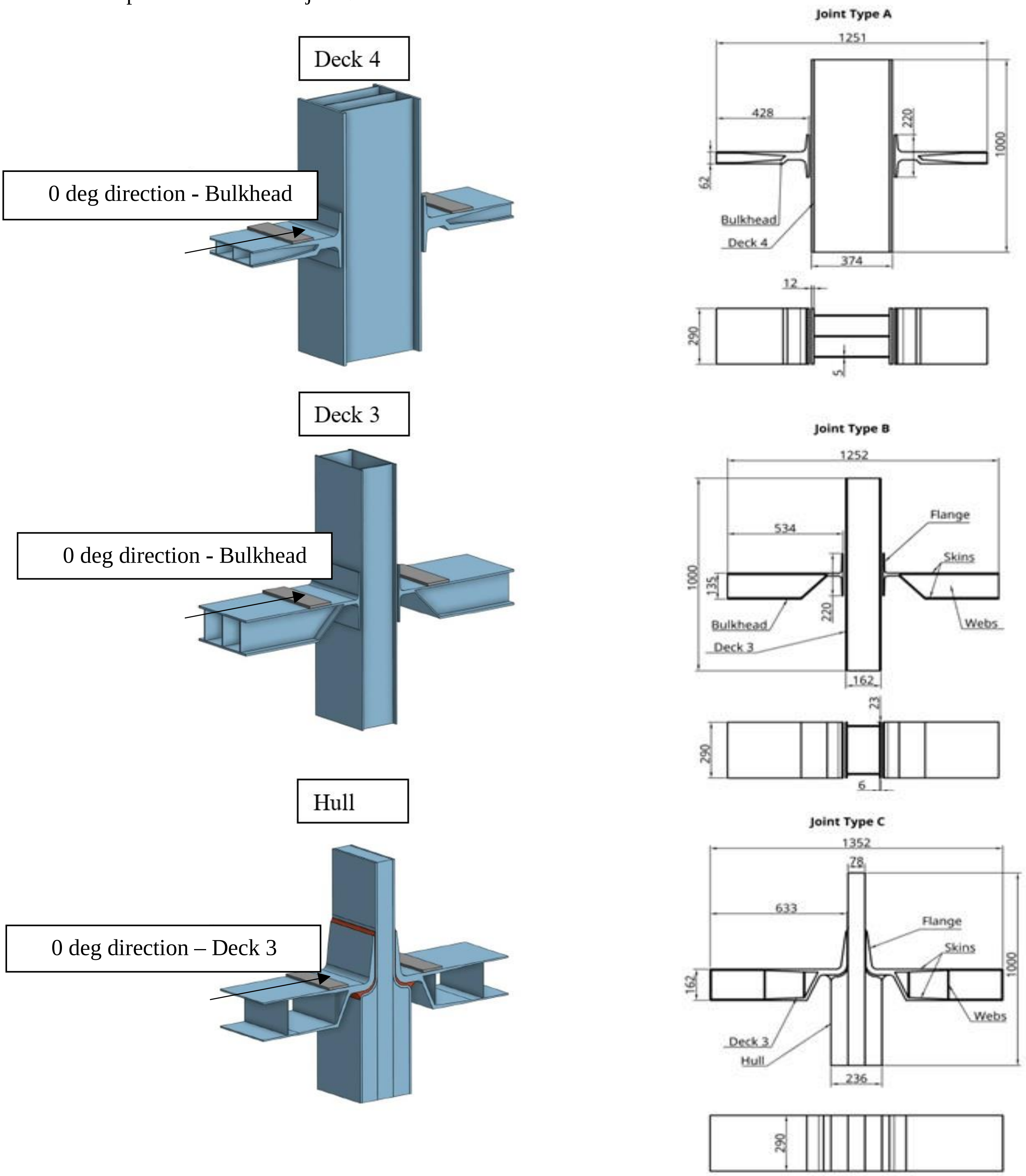

Figure 2 –Test specimens; Left: Type A (between deck 4 and bulkhead); Centre: Type B (between deck 3 and bulkhead); Right: Type C (between deck 3 and hull)

Figure 3 – 5-point-bending test setup with Specimen Type C

Figure 4 – Close up view of the load cylinder; load introduction via a ball joint; load distribution via steel plate and wooden plank

2.3 Instrumentation

Several failure modes can occur in such connections under the given load configuration; substrate failure (i.e. failure in the composite adherents) can occur as fibre tear, matrix cracking, interlaminar failure (i.e. delaminations); cohesive failure can occur within the adhesive itself. The unacceptable failure mode is interface failure (i.e. adhesive failure) in between the two materials. This failure mode generally indicates errors in the bonding procedure.

In order to evaluate the structural performance of the joints, one piece of information to collect is the force exerted by the load cylinder. It is needed to calculate the shear strength of the adhesive and the interlaminar shear strength of the composite. In addition, surface strain values are needed to identify failure initiation locations. The strains can be used to compute stress. At the same time, the stress values can provide a verification of the value computed from maximum load registered by the cylinder. Finally, visual inspection provides insight into occurring failure mechanisms in terms of initiation, progression, and ultimate failure. In the experiments, force and displacement (stroke) data is provided via the load cylinder and it is continuously recorded during the experiment. Additional information is collected using a 3D Digital Image Correlation (DIC) system. This is an optical technique that is used to collect local strain data. The technique is based on surface analysis methods which involve monitoring and identifying changes in a pattern of points applied to the surface of the object of interest. The output comes in the form of a recording of the strain field along the cross section of the specimen. In this study, it is used to record the relative displacements between adherents and adhesive, to identify potential interfacial failure, and between the plies of the laminate itself, for potential substrate failure. The areas of interest of the cross section are shown in Figure 5. The quality of the measurements is dependent on the quality of the speckle pattern and the size of the speckles. An ideal pattern should have an average size equal to 3-5 times the image pixel size and should have limited scatter in speckle size [8].

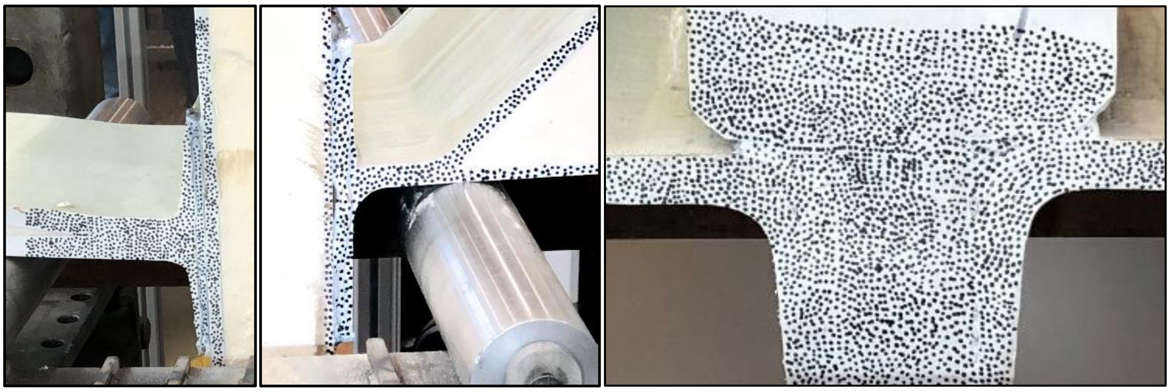

Figure 5 – DIC speckle pattern on test specimens; From Left to Right: Type A, B and C

3 NUMERICAL INVESTIGATION

Following the experimental study, numerical simulations are performed on the three specimen designs. A finite element model (FEM) of the joint design is created. Validated models are important to vary the design in a numerical environment and allow for multiple iterations without the need to repeat experiments at this scale. The finite element analysis (FEA) is performed in Abaqus/CAE 2019 software [9] using 8-noded SC8R linear, quadrilateral, continuum shell elements for the laminates and 8-noded C3D8R linear, brick elements for the adhesive. Further details regarding these element types are given in the Abaqus documentation [9]. Mesh refinement is performed to determine the optimum number of elements through the thickness of the adhesive and the portion of the mesh beyond the end of the bond line that requires fine mesh to capture stress peaks (see Figure 6). Five elements are used in the thickness of the adhesive to ensure stress gradients can be captured.

Based on the experimental observations, it is known that several failure modes on these joints can be expected. The failure modes these models should capture are substrate failure close to the interface, delamination of the flange laminates or adhesive failure. For the model to capture these possible failure modes, cohesive zone modelling technique is used. Two interface properties are defined, namely FRP-FRP and FRP-Adhesive.

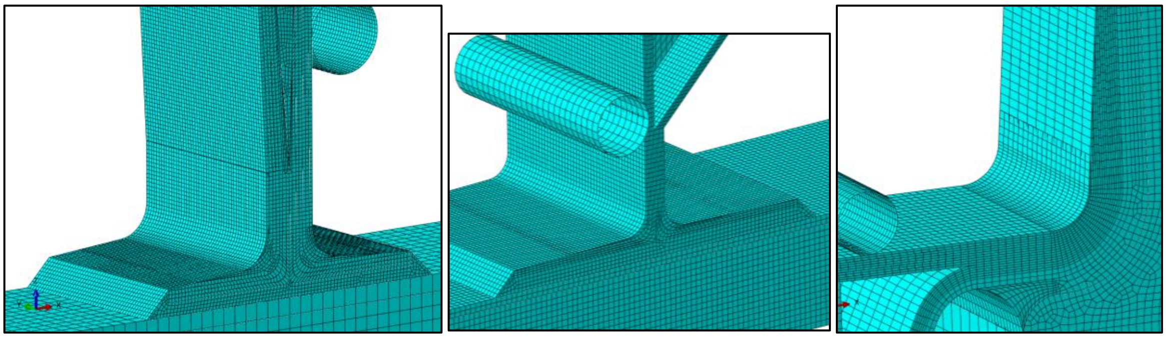

Figure 6 – Mesh on Joint models. From Left to Right: Type A, B and C

Related to the materials, for the FRP, UD lamina properties are used as homogenous, orthotropic base material. The laminates are built up in their respective stacking sequence using the UD lamina properties for each layer. The adhesive has a hyperelastic constitutive model which is introduced in Abaqus in the form of the stress-strain curve resulting from an uniaxial test on the bulk material. Duncan and Crocker [10] show that good accuracy can be obtained by only utilizing uniaxial and volumetric test data while also presenting a way of deriving the later from the former. This means that the uniaxial test result stress-strain curve is sufficient for a complete description of the behavior of a hyperelastic material.

The mechanical properties used for both the FRP material model and the damage models are given in Table 1 and

Table 2 and are obtained from material level tests within the RAMSSES project, reproduced in the current research, while the properties for the adhesive material model have been provided by the manufacturer and are shown in

Table 3 and

Table 4. The load is applied at the top of the central part, in displacement control, similar to the experimental setup. Dimensions are identical to the ones used during the experiment phase.

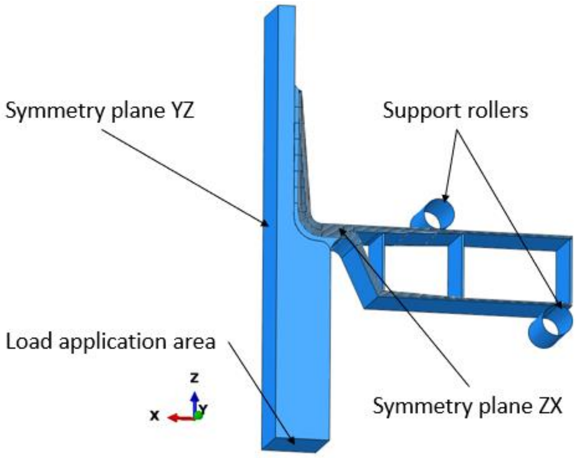

Figure 7 – Boundary conditions of Joint Type C; analogous for joint Type A and Joint Type B

In relation to the boundary conditions, because only a quarter model is used, two symmetry planes are specified (i.e. along the YZ and XZ planes as shown in Figure 7). Two support rollers are modelled as rigid bodies and constrain the movement in vertical direction while allowing the specimen to slide. The results of interest are the reaction force vs. displacement curve and the predominant failure mode is of interest, together with post-failure behaviour.

Property	Notation	Unit	Value	Source
Density	ρ	ton/mm^3	1.8E-09	DIN EN ISO 1183-1, method A
E moduli	E1	MPa	34860	DIN EN ISO 527
	E2	MPa	11984	DIN EN ISO 527
	E3	MPa	11984	=E22*
Poisson's ratios	ν12	(-)	0.24	DIN EN ISO 527
	ν13	(-)	0.24	=ν12*
	ν23	(-)	0.35	Theory Hashin
Shear moduli	G12	MPa	3723.5	DIN EN ISO 14129:1997, tensile test
	G13	MPa	3723.5	=G12*
	G23	MPa	1500	Theory Hashin

* Under the assumption of transverse isotropy

Table 1 - elastic, orthotropic, homogenous properties for UD glass fiber lamina

Interaction type	Interaction property	Interaction parameter	Unit	Value
Tangential behaviour	Penalty	Friction parameter	(-)	0.3
Normal behaviour	Hard contact	(-)	(-)	(-)
		$k_n = k_I = E_{resin} / t_{resin}$	N/mm^2/mm	30000

Cohesive behaviour	Traction separation behaviour	$k_s = k_{II} = G_{resin} / t_{resin}$	N/mm^2/mm	11550
		$k_t = k_{III} = k_s$	N/mm^2/mm	11550
Damage initiation	Quadratic criterion	(-)	(-)	(-)
	Maximum nominal stress	Normal Only	MPa	15
		Shear-1 Only	MPa	27
		Shear-2 Only	MPa	27
Damage evolution	Type	Energy		
	Softening	Linear		
	MM behaviour	Benzeggagh-Kenane		
	MM ratio	Energy		
	Exponent			2.28
	Damage evolution values	Fracture energy Mode I: G_{IC}	J/mm^2	1.64
		Fracture energy Mode II: G_{IIC}	J/mm^2	1.46
		Fracture energy Mode III: G_{IIIC}	J/mm^2	1.46

Table 2 – FRP-FRP interaction property parameters

Property	Notation	Unit	Value	Source
Density	ρ	ton/mm^3	1.12E-09	Datasheet Scigrip
E modulus	E	MPa	241.5	Datasheet Scigrip
Poisson's ratio	ν	(-)	0.48	Datasheet Scigrip
Shear modulus	G12	MPa	2012.5	Datasheet Scigrip

Table 3 - hyperelastic, orthotropic, homogenous properties for adhesive

Interaction type	Interaction property	Interaction parameter	Unit	Value
Tangential behaviour	Penalty	Friction parameter	(-)	0.3
Normal behaviour	Hard contact	(-)	(-)	(-)
Cohesive behaviour	Traction separation behaviour	$k_n = k_I = E_{adhesive} / t_{adhesive}$	N/mm^2/mm	24.15
		$k_s = k_{II} = G_{adhesive} / t_{adhesive}$	N/mm^2/mm	8.15
		$k_t = k_{III} = k_s$	N/mm^2/mm	8.15
Damage initiation	Quadratic criterion	(-)	(-)	(-)
	Maximum nominal stress	Normal Only	MPa	12
		Shear-1 Only	MPa	16
		Shear-2 Only	MPa	16
Damage evolution	Type	Energy		
	Softening	Linear		
	MM behaviour	Benzeggagh-Kenane		
	Exponent			2.28
	Damage evolution values	Fracture energy Mode I: G_{IC}	J/mm^2	1.64
		Fracture energy Mode II: G_{IIC}	J/mm^2	1.46
		Fracture energy Mode III: G_{IIIC}	J/mm^2	1.46

Table 4 – FRP-Adhesive interaction property parameters

4 RESULTS AND DISCUSSION

As shown in the previous sections, test specimens for three different joint designs are built and tested, followed by a numerical study aiming to correlate the experimental results. The current chapter shows and discusses these results in detail.

4.1 Experimental results

The 5-point-bending experiments are performed and the force displacement graphs shown in Figure 8, Figure 11 and Figure 14 are obtained for the three different joint types. For each joint type, one specimen is tested in 3-point-bending before identifying that unrealistic rotations occur in this situation. The setup was improved, and these specimens were tested again. The re-tested specimens are the ones that behave differently from the other two in for each set. (i.e. lower maximum force and/or lower stiffness).

Specimen Type A

For Joint Type A, for two of the specimens (i.e. A1 and A2), the load increases linearly with the displacement until 40 to 50kN (i.e.33-49 N/mm). Afterwards, with increasing load, deviation from non-linearity occurs. This is caused by internal cracks in the deck, at the interface between skins and webs which result from the relatively large stiffness difference between the thick foot of the bulkhead and the thin deck laminates.

The highest load is recorded in specimen A3. It has been observed that the high stiffness difference between the bulkhead and deck results in a high sensitivity of the specimen to alignment of the support rollers. Small misalignments can cause large peak stresses to initiate in the corner of the joint which then opens suddenly due to the large stiffness of the bulkhead flange. This caused the first two specimens to fail at a lower load than the third one.

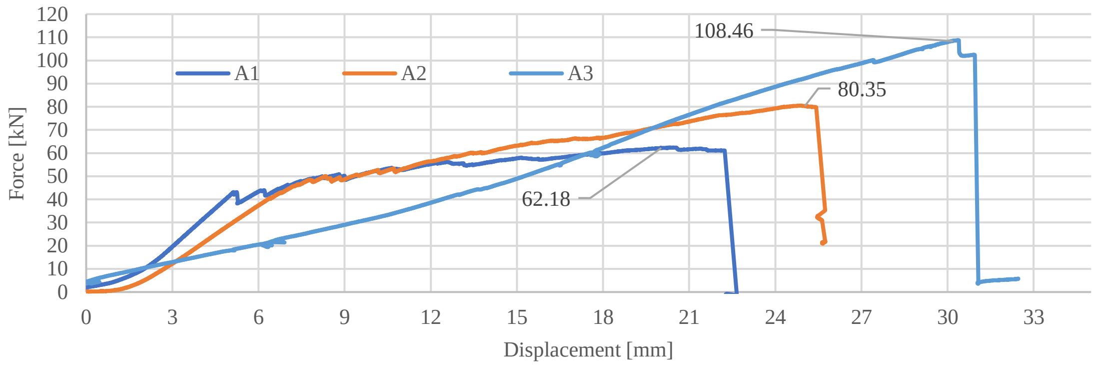

Figure 8 – Load-displacement curve of joint Type A

Figure 9 – Specimen A3: Left: Front view; shear failure on the deck laminate highlighted in red; Right: Back view; laminate damage highlighted in red lines.

Figure 10 – Failure plane of A3; Top: Flange of the bulkhead; Bottom: Adhesive on deck side.

For joint Type A, the failure mechanism is as follows. First, damage initiates internally, in the deck as matrix cracking at the interface between skin and webs. These events are found in the nonlinear portion of the force-displacement diagram as small, subsequent drops in force. Next, at higher loads, delaminations occur in the foot of the bulkhead, initiating near the corner, on the tension side, and then propagating towards the end of the flange as shown in Figure 9. Failure occurs by partial substrate failure combined with adhesive failure at the bulkhead adhesive interface, as can be seen in Figure 10. Due to lack of perfect symmetry between the two joints of the specimen, one of them fails before the other. Furthermore, due to the large thickness of the central element (deck), there is no influence of the failure of one joint on the other.

Specimen Type B

In the case of Joint Type B, load increases linearly with the displacement up to 80 to 90kN (i.e. 67-75 N/mm). Afterwards, a sharp drop is recorded, followed by a slow increase in load with increasing displacement. This is caused by failure in the flange of the bulkhead at the tension side followed by a shift in the load transfer mechanism of the joint. The force in the joint is now primarily taken up by the shear and compressive strength of the remaining portion of the flange of the bulkhead. The subsequent increase in load can be interpreted as further signaling of damage and adds to the robustness of the join. For the purposes of the current research, this residual load is not considered. The joint is assumed to be failed at this point. The highest load is recorded in specimen B3, with the rest of the specimens also reaching a similar maximum force at comparable displacement levels.

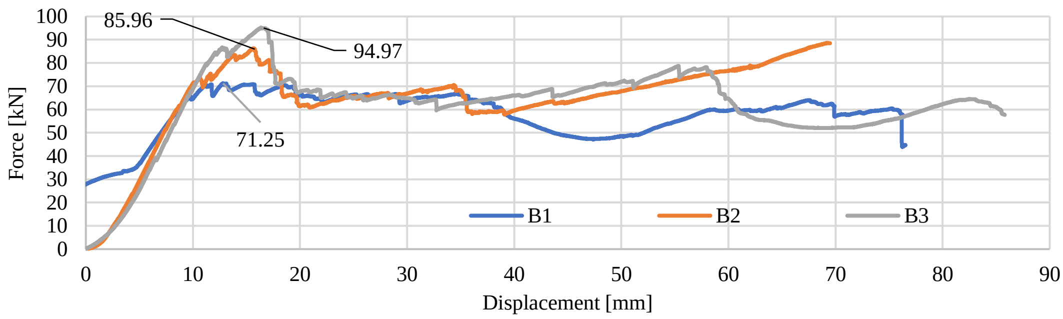

Figure 11 - Load-displacement curve of joint Type B

Figure 12 – Specimen B3: Left: Front view; Failure initiation; Right: Front view, Ultimate failure.

The following failure mechanism occurs in joint Type B. First delaminations initiate at the point where the two skins of the bulkhead join (see

Figure 12), and progress towards the joint (interlaminar shear strength is reached quickly due to the relatively thin laminate in the foot). Subsequent delaminations occur in the lower half of the laminate and propagate towards the end (see

Figure 12**Error! Reference source not found.**). Ultimate failure occurs in the form of delaminations of the foot of the bulkhead. If the load can still increase, the bulkhead disconnects from the joint by fiber tear (

Figure 12). Once delaminations propagate until the end of the flange at the bottom side, the load mechanism changes. The upper part of the flange starts to carry the load by compression in the fibers and shearing of the adhesive.

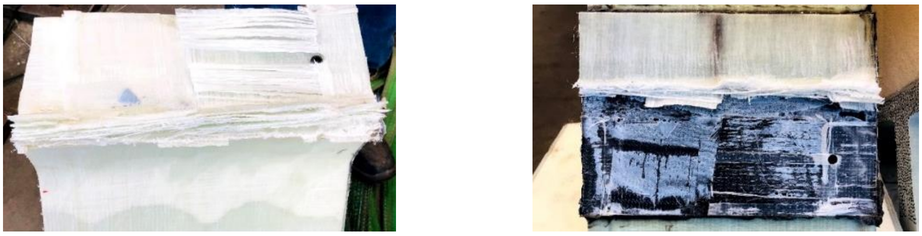

Figure 13 – Specimen B2: Post failure inspection; Left: Flange of the bulkhead; Right: Deck side.

Specimen Type C

For Joint Type C, load increases linearly with the displacement until 60 to 70kN (i.e. 50-58 N/mm). Afterwards, under relatively constant load, displacement increases significantly. This is caused by subsequent delaminations in the deck flange which allows for rotation of the joint. The highest load is recorded in specimen C2. The remaining two specimens behave similarly and reach comparable maximum loads.

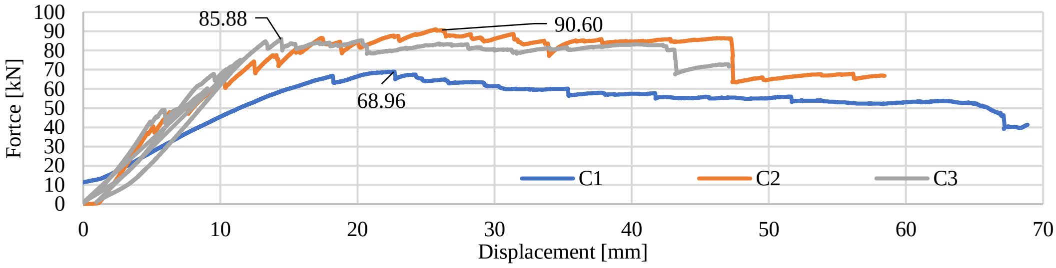

Figure 14 - Load-displacement curve of joint Type C

The following failure mechanism takes place for joint Type C. First, delaminations originate in the corner of the deck and propagate downwards, towards the end of the flange.

The first delamination occurs towards the centre of the flange in thickness direction. Subsequent delaminations happen at the centre of the undamaged areas (i.e. locations where interlaminar shear stress is largest). Once delaminations propagate to the end of the flange at the bottom side, the capacity drops. Ultimate failure occurs when the joint is no longer capable of carrying additional load. This happens when sufficient delaminations occur. Although the flange can still carry some load in tension once a large enough angle has been achieved; this is not representative of a realistic situation, however, it proves the flexibility of the joint and the multiple load paths available.

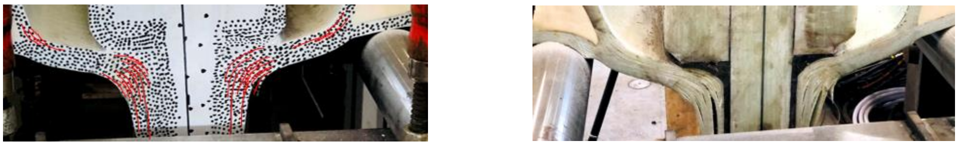

Figure 15 – Specimen C3: Left: Front view: laminate damage; Right: Back view.

4.2 Numerical results

The numerical results are presented for each specimen type in terms of Force versus displacement graphs, superimposed over the corresponding experimental ones. Furthermore, qualitative assessment of the damage mechanism is formulated for each specimen type. Where applicable, parallels are drawn between the experimental and numerical results.

Specimen Type A

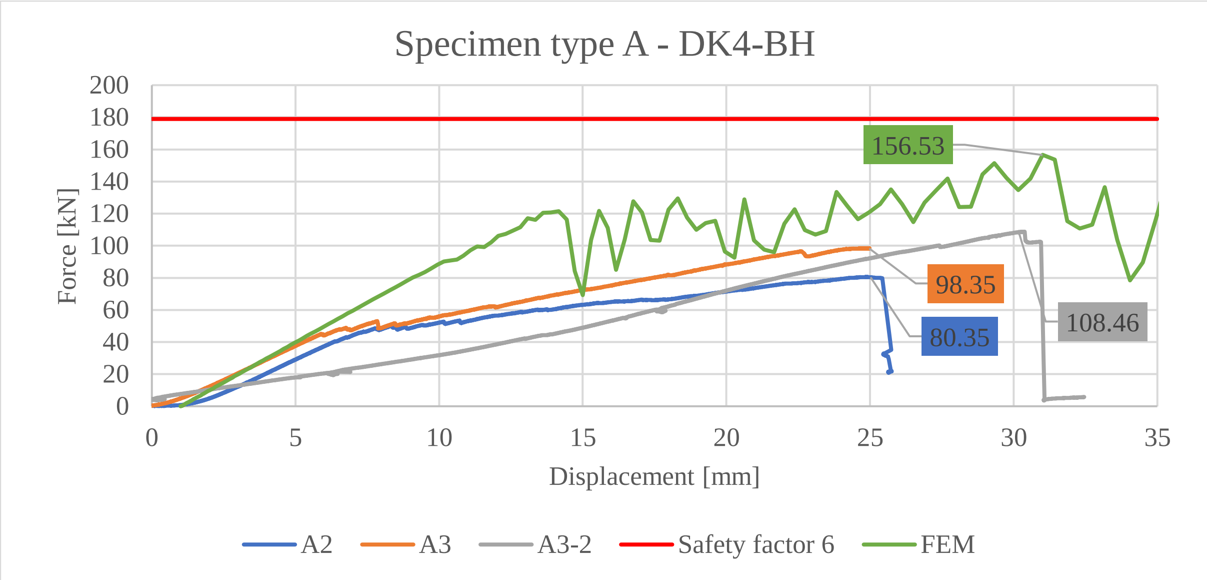

Figure 16 – F-d graph: Joint Type A

The initial stiffness matches perfectly between experiment and FEA. In the experiment curves, a distict change in the slope is recorded. This has been associated with internal damage of the deck, at the skin web interface, as a result of the joint rotation. As covered in the limitations chapter, this failure mode has not been characterised and implemented in the model and as a result, this phenomenon does not occur in the FEA.

As a result, from this point, the FEA diverges from the experiments. The load is able to increase in the model to around 120 kN at which point delaminations occur in the foot of the bulkhead. Following the initial delaminations, the load can still increase slightly (i.e. to around 150kN).

In contrast, during the experiment, since the skin-web interface was damaged, the ultimate load was around 110 kN. No damage of the joint occurred. Instead, all Type A specimens failed by interfacial failure at the deck-adhesive or at the bulkhead adhesive interface. Shortly after the experiments, it has been determined that the supports were slightly missaligned which, in the case of such a stiff connection, caused even a small failure initiation to propagate quickly across the entire surface of the joint and cause debonding.

	Experimental avg.	**Numerical**	**Difference**
Ultimate load [kN]	95	156	61%

The misalignment of the supports which results in asymmetric loading of the connection and implicitly, the deck can be the reason for the skin-web debonding. One of the three webs from one specimen can be loaded more severely than the rest. In the numerical model, the load and boundary conditions are implemented symetrically.

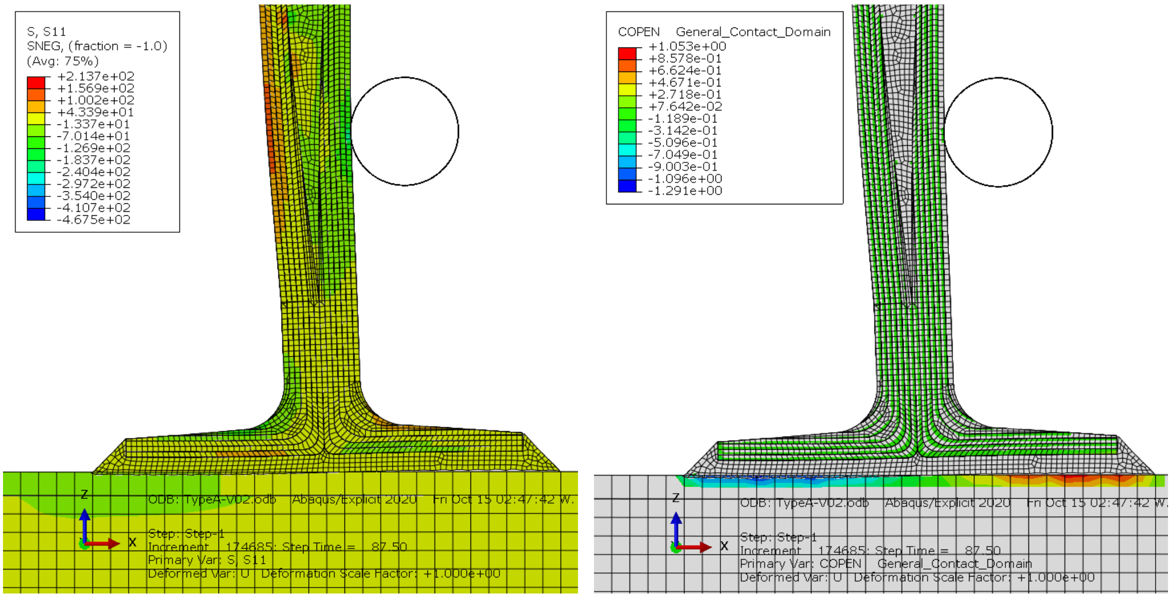

Figure 17 – FEA: Failure mechanism: Failure initiation – interfacial failure; Top: Von Mises stress; Bottom: Contact opening (Gap: opening occured; Red: next location where opening will likely occur; Blue: opening unlikely to occur)

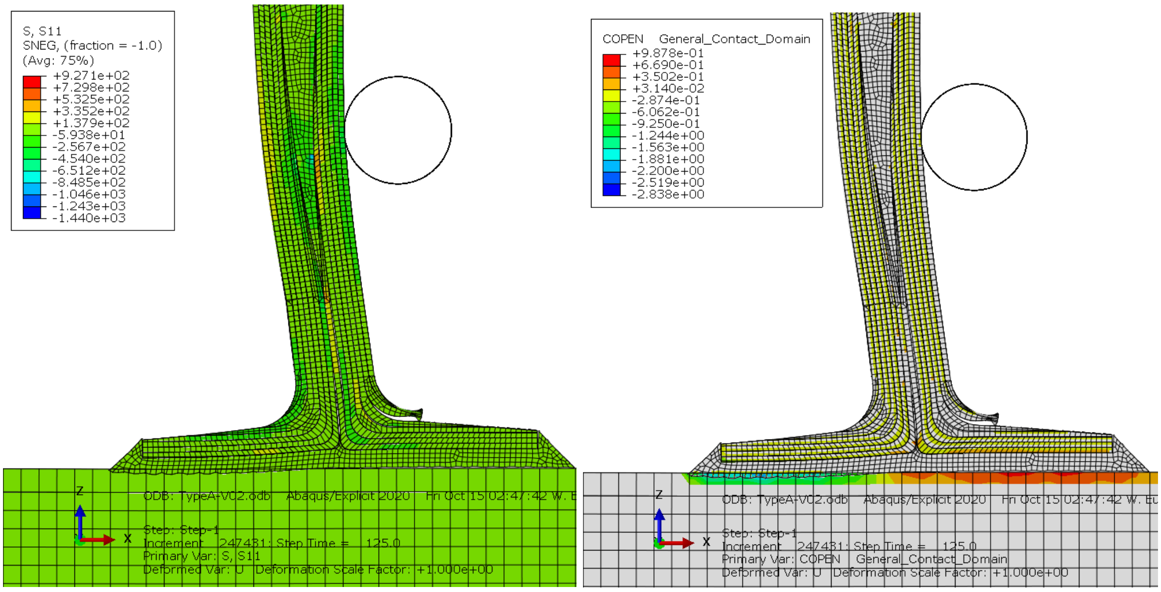

Figure 18 – FEA: Failure mechanism: Failure process – delamination initiation near inner corner

The failure mechanism in terms of joint behaviour is captured with reasonable accuracy. Both interfacial failure between deck and adhesive, as well as laminate damage in the foot of the joint are present in the model. The main difference, as outlined above, is that, due to symmetry, the partial debonding of the interface does not cause failure of the joint.

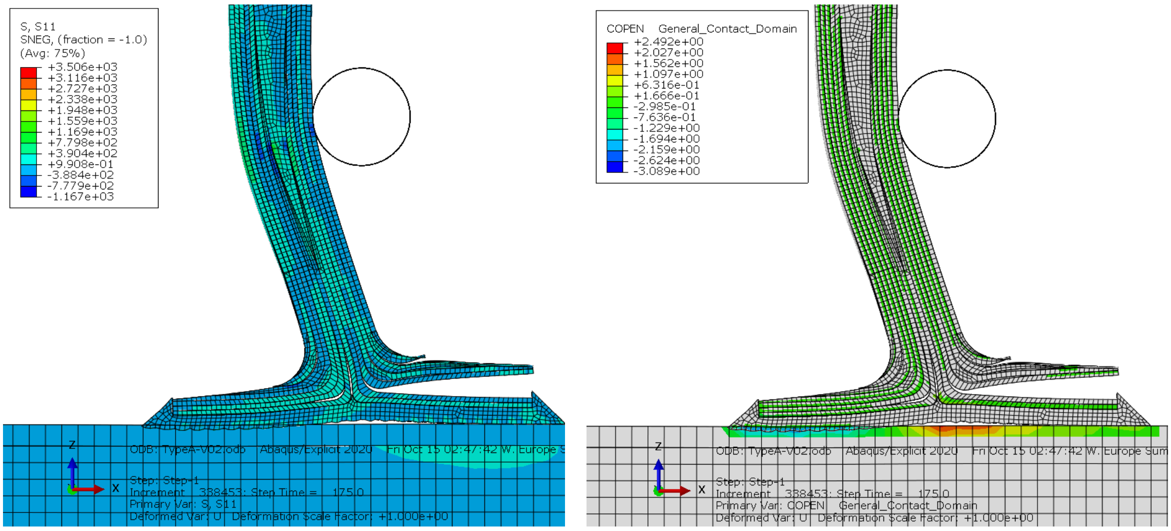

Figure 19 – FEA: Failure mechanism: Failure process – delamination at the center of the flange of the bulkhead

Specimen Type B

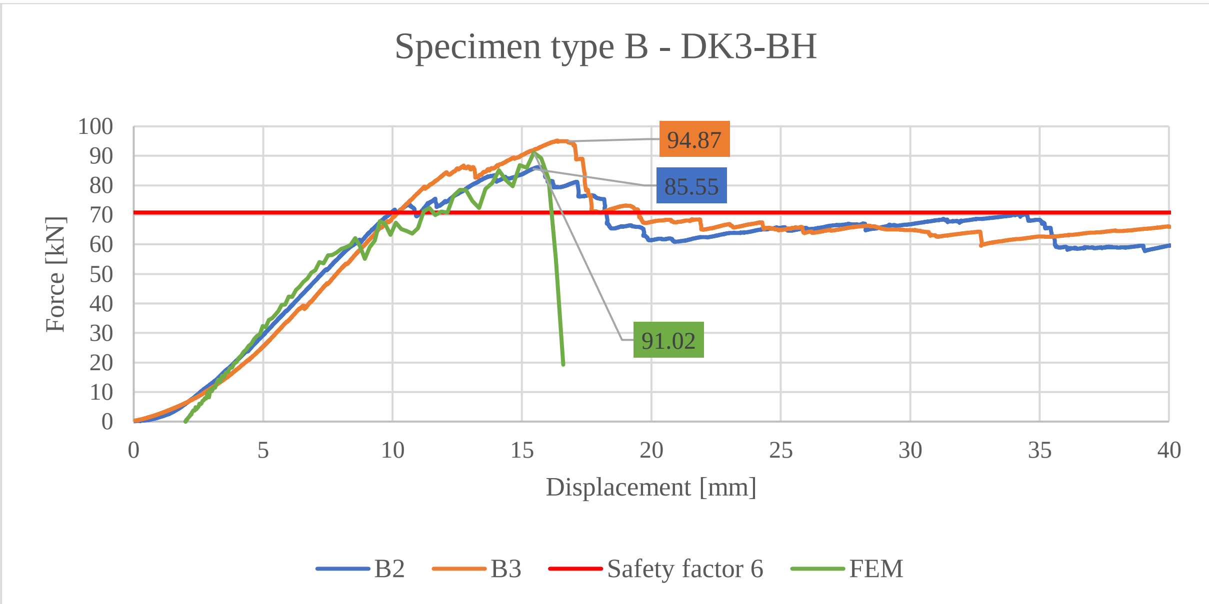

Figure 20 – F-d graph: Joint Type B

The initial stiffness matches almost perfectly between experiment and FEA. The small drops in the FEA result are caused by subsequent delaminations. Reductions in stiffness are also captured. Ultimate load is similar between experiment and FEA. The force in the numerical model drops to almost 0 after reaching ultimate load, meaning that post failure behaviour cannot be captured.

	Experimental avg.	**Numerical**	**Difference**
Ultimate load [kN]	90	91	0.1%

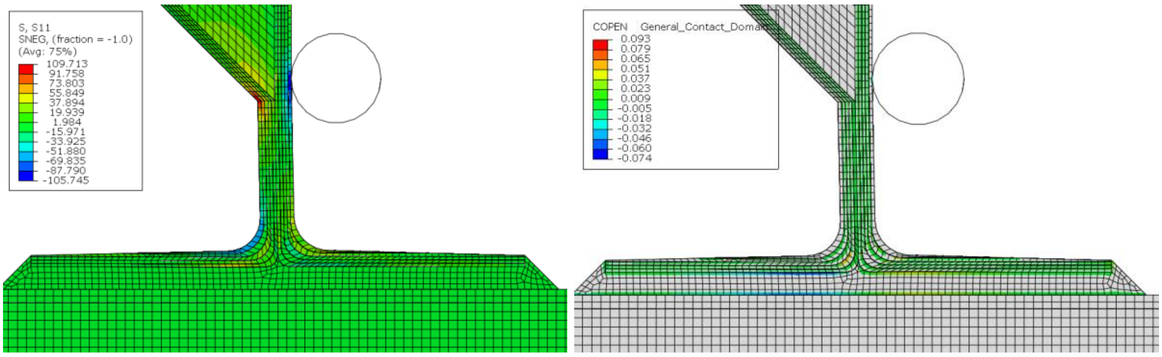

Figure 21 – FEA: Failure mechanism: Failure initiation; Left: S11; Right: Contact opening (Gap: opening occured; Red: next location where opening will likely occur; Blue: opening unlikely to occur)

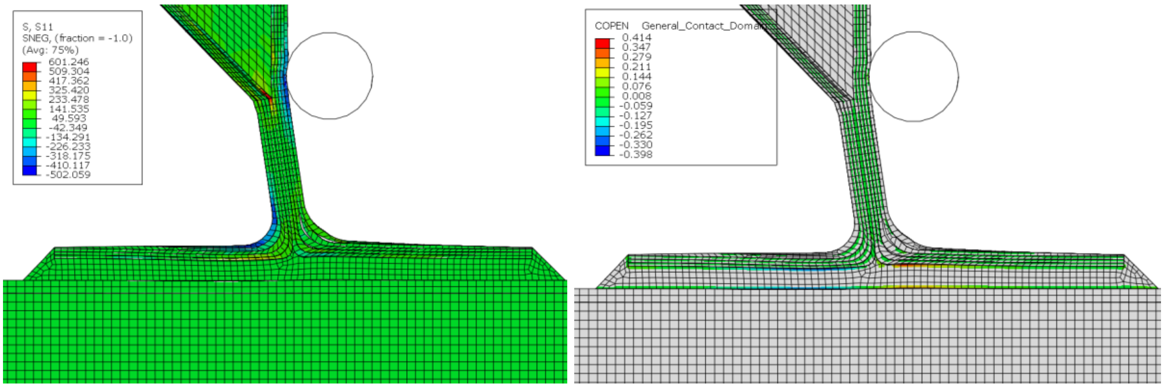

Figure 22 – FEA: Failure mechanism: Ultimate failure; Left: S11; Right: Contact opening (Gap: opening occured; Red: next location where opening will likely occur; Blue: opening unlikely to occur)

Failure mechanism is consistent with the experiment. Delaminations initiate in the foot of the bulkhead, near the center in thickness direction. Subsequently, they propagate into the flange, on the tensile side.

Ultimate failure occurs in the experiment following a change in the load transfer mechanism once the tension side flange looses load capacity. The numeric model cannot reach this far into the failure process due to severe discontinuities.

No damage occurs in the adhesive or in the deck component.

Specimen Type C

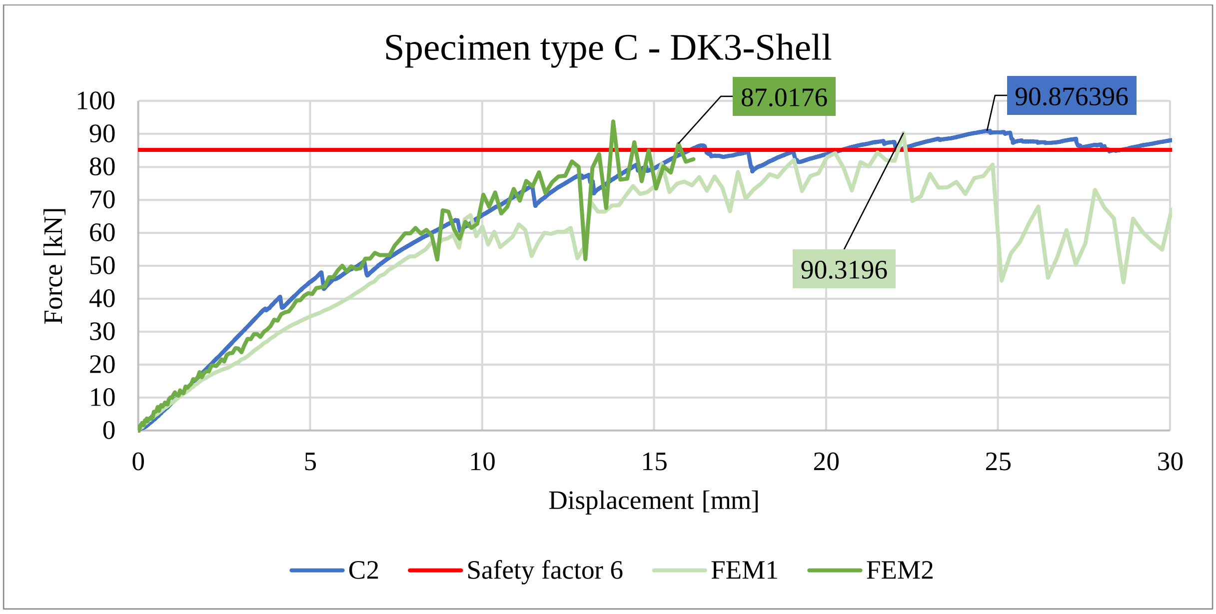

Figure 23 – F-d graph: Joint Type C

In the case of Joint Type C, buckling of the web directly under the load application are has been observed initially. This is caused by the fact that during the experiment and FEM the load is introduced over a short distance for practical reasons, with the only aim to have the correct shear force and bending moment combination at the joint. In reality a smaller distributed load is applied over the entire deck. As a result, PU blocks were included in the model.

The initial stiffness matches with reasonable accuracy in the first portion of the graph. The small, distinct drops followed by stiffness reduction in the experimental graph are associated with small delaminations initiating in the flange. The FEA does not follow each subsequent drop, however the overall slope of the graph is decreasing at a similar rate. This is explained by a combination of the element size, sub-laminate size and initiation fracture energy specified in the damage model. Overall, the stiffness is well predicted.

The ultimate load is underestimated in the FEM without PU blocks due to the buckling event reducing the load bearing capacity. Addding the PU blocks increases the resistance of the joint in this load configuration but it causes more issues with contact, interaction and connectivity between elements which results in the “oscillation” of the graph near the end. This can be solved by increasing the analysis time, however the added benefit would be minor, as the significant properties are matced with sufficient accuracy.

	Experimental	Numerical	Difference
Ultimate load [kN]	91	87	4.4%

The failure mechanism is consistent with the experiment. Delaminations occur in the flange of the deck. They initiate near the center in thickness direction, due to the high interlaminar shear stresses. Then, several more failure planes open, towards the inside of the angle. Cracks propagate towards the deck and towards the end of the flange.

Ultimate failure occurs when not enough flange thickness remains to transfer the deck load. No damage occurs in the adhesive or in the hull.

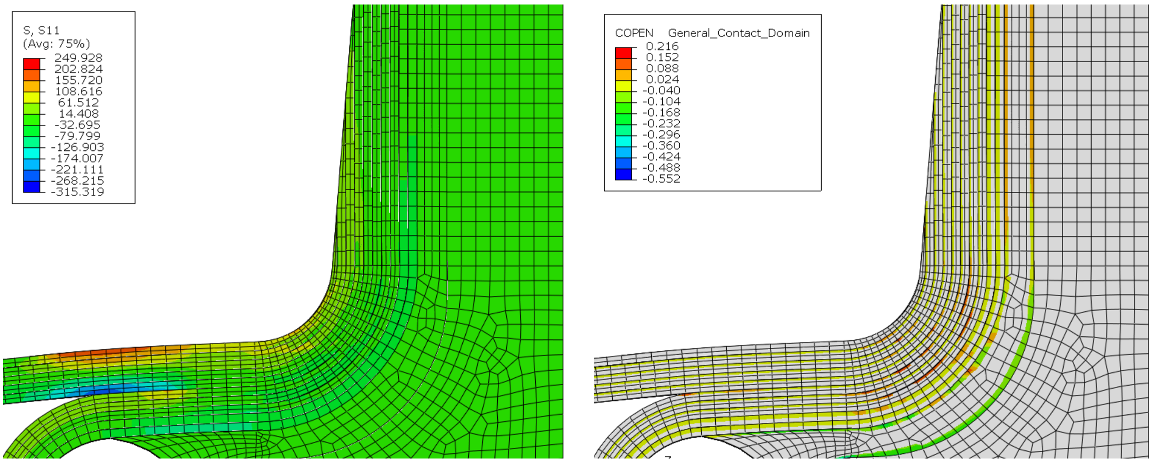

Figure 24 – FEA: Failure mechanism: Failure initiation Left: S11; Right: Contact opening (Gap: opening occured; Red: next location where opening will likely occur; Blue: opening unlikely to occur)

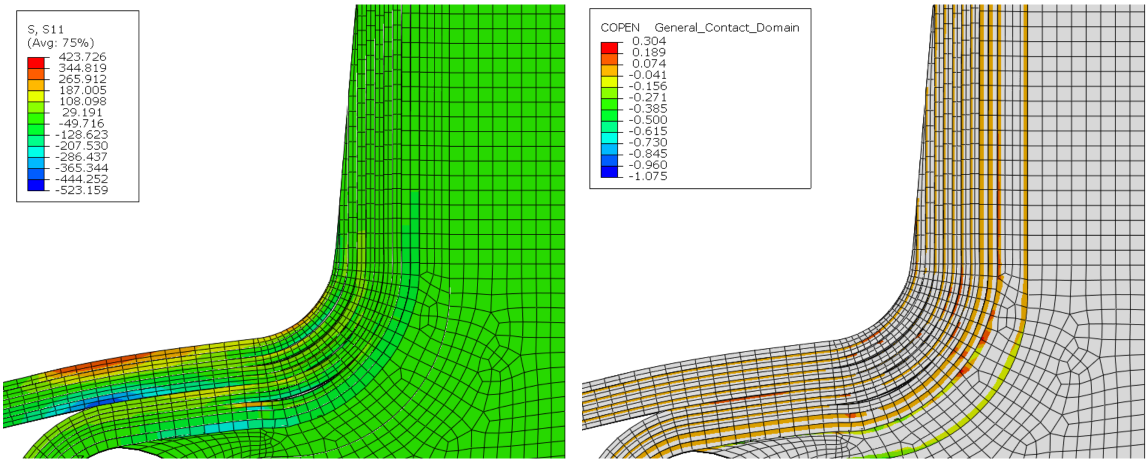

Figure 25 – FEA: Failure mechanism: Several delamination planes occurred

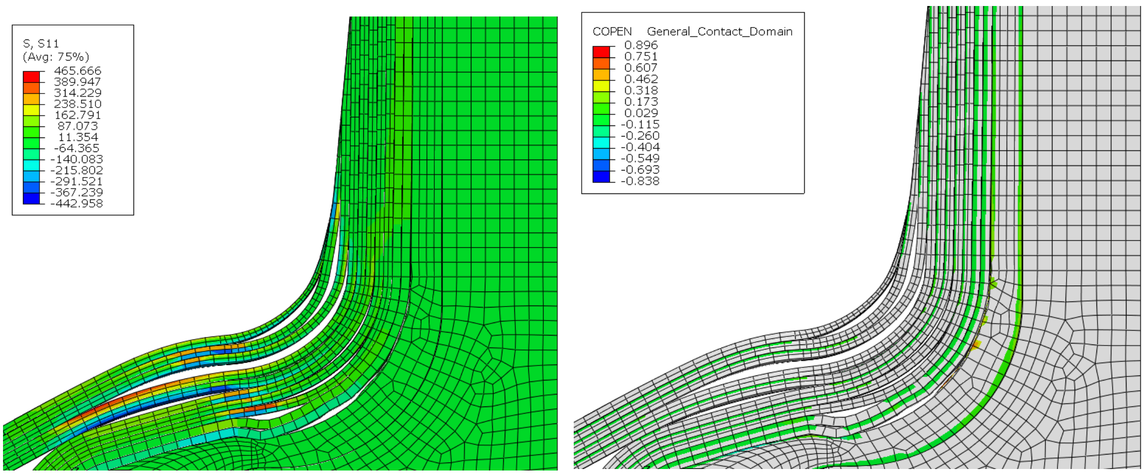

Figure 26 – FEA: Failure mechanism: Ultimate failure

5 CONCLUSIONS

Three different joint designs were developed and tested, both at an experimental, as well as a numerical level. They were designed based on real-life loads acting on a 85 m-long full composite vessel that complies with Safety of Life at Sea (SOLAS).

The experimental portion of the study focused on obtaining representative specimen dimensions and test setup in order to ensure realistic failure mechanisms are engaged. Five-point-bending proved to constrain the specimen sufficiently to bring the required shear load into the joint without generating an unrealistically large bending moment. Furthermore, the design load imposed by classification was the target each joint should reach before failure.

The numerical study resulted in three models that are able to predict the behaviour of three different adhesive joints between composite panels with good accuracy, as long as the failure mechanisms of interest are included.

The models for joint Type B and Type C replicated what was observed during the experiment closely. The ultimate load is within 5% of the experimental values, while the failure process is also captured. The location of initiation, direction of propagation and moment of ultimate failure are realistic. The model for joint Type A was able to overcome one of the limitations that often comes with experiments, namely the sensitivity of the speciment to the test setup. The testing conditions can sometimes be off by a small manner and in doing so, causing undesired loading for which the specimen is not designed. This can result in premature failure by a different failure mode than expected. The model was able to predict a better joint behaviour as a result of removing the effects of asymmetric loading and show that the joint functions as intended with the laminate being the critical component of the joint, and not the interfaces.

REFERENCES

[1] C. Smith, Design of Marine Structures in Composite Materials 1st Edition, Elsevier, 1990.

[2] RAMSSES, "Custom-made hull," RAMSSES, 10 2020. [Online]. Available: https://www.ramsses-project.eu/. [Accessed 28 10 2020].

[3] Bureau Veritas, "Bureau Veritas," 2020. [Online]. Available: https://group.bureauveritas.com/. [Accessed 28 10 2020].

[4] J. R. Weitzenböck, "1 - Introduction to using adhesives in marine and offshore engineering," *Adhesives in Marine Engineering,* pp. 1-16, 2012.

[5] R. Y. L. X. Haiyan Zenga, "Failure prediction of composite sandwich L-joint under bending," *Composite Structures,* vol. 197, pp. 54-62, 2018.

[6] DAMEN SCHELDE NAVAL SHIPBUILDING, "DAMEN SCHELDE NAVAL SHIPBUILDING," 2020. [Online]. Available: https://www.damen.com/companies/damen-schelde-naval-shipbuilding. [Accessed 28 10 2020].

[7] InfraCore Company, "InfraCore Company," 2020. [Online]. Available: https://infracore-company.com/. [Accessed 28 10 2020].

[8] M. Sutton, M. Cheng, W. Peeters, Y. Chao and S. McNeill, "Application of an optimized digital correlation method to planar deformation analysis method to planar deformation analysis," *Image and Vision Computing,* vol. 4, no. 3, pp. 143-150, 1986.

[9] Dassault Systèmes Simulia Corp, "Abaqus/CAE User's Manual," 2011. [Online]. Available: http://130.149.89.49:2080/v6.11/pdf_books/CAE.pdf. [Accessed 10 01 2021].

[10] B. Duncan and L. Crocker, Characterisation of Flexible Adhesives for Design, Teddington: Crown, 2001.